

# Numerical Simulation of High-Speed Flows Over Complex Geometries with a High-Order Multi-Zone Cut-Cell Method

Patrick T. Greene\*, Jeff D. Eldredge<sup>†</sup>, Xiaolin Zhong<sup>‡</sup> and John Kim<sup>§</sup>

*University of California, Los Angeles, CA, 90095-1597, USA*

Results are presented for a new code designed to perform high-order direct numerical simulations of high-speed flows over arbitrary geometries. The simulations were performed on a Cartesian grid with the geometries imposed by a third-order cut-cell method. A multi-zone refinement method is also implemented to provide extra resolution at locations with expected complex physics. The simulations also utilize a fifth-order hybrid WENO scheme to capture any steep gradients in the flow created by the geometries. The combination results in a globally fourth-order scheme. Two-dimensional and three-dimensional test cases show good agreement with previous results and will be presented. Results confirming the high order of convergence will also be shown. The code was designed for studying the effects of isolated roughness elements on the stability of hypersonic boundary layers. Preliminary results for Mach 6 flow over a three-dimensional cylindrical roughness element will also be presented.

## I. Introduction

THE ability to accurately predict the location of laminar to turbulent transition in boundary layers is of great importance to the design of hypersonic vehicles. At high Mach numbers, the viscous effects in the boundary layer can cause extreme surface temperatures as kinetic energy is converted to thermal energy. When the flow transitions from laminar to turbulent, this heating is further increased by turbulent mixing near the wall. In addition to the thermal effects, turbulent flow also generates larger shear stresses which increase the friction drag on the surface. Without the knowledge of the transition location, designers of hypersonic vehicles must be overly cautious with their designs. Thermal protection and propulsion systems must assume turbulent flow over the entire body.<sup>1</sup> In spite of its importance, the mechanisms leading to the transition of hypersonic boundary layers are still poorly understood.<sup>2</sup> Predicting the location of transition is further complicated by the presence of surface roughness.

The effects of roughness elements have been documented for sometime experimentally. Schneider<sup>2</sup> has recently written a review of experiments studying the effect of roughness on hypersonic boundary-layer transition. Roughness elements generally cause the location of transition to move upstream compared to flow without a roughness element. It is possible to have a small enough roughness element such that there is no effect on the transition location. Such a roughness is said to be below its critical height. Only a roughness element above this critical height will cause a change in the transition location. As the roughness height is increased past this critical height, the location of transition will continue to move closer to the roughness element. Eventually transition will occur at its closest location downstream of the roughness. This location may still be a finite distance downstream of the roughness. Further increases of the roughness height will no longer cause the transition location to move forward. The height at which this occurs is called the effective height. Although a great deal of research has been done to study the effects of roughness on hypersonic transition, most of the data was for correlations to be used in the design of hypersonic vehicles. Very

\*Graduate Student, Department of Mechanical and Aerospace Engineering, greene@seas.ucla.edu, AIAA Student Member.

<sup>†</sup>Associate Professor, Department of Mechanical and Aerospace Engineering, AIAA Associate Fellow.

<sup>‡</sup>Professor, Department of Mechanical and Aerospace Engineering, AIAA Associate Fellow.

<sup>§</sup>Professor, Department of Mechanical and Aerospace Engineering, AIAA Member.

little is actually known about the exact physics behind hypersonic boundary-layer transition with roughness elements.

In the recent past, a great deal of work went into exploring transient growth as an important role in roughness-induced transition. Tumin and Reshotko<sup>3</sup> presented a spatial theory for transient growth in boundary-layer flow. They showed that the most significant transient growth is associated with steady streamwise vortices. Roughness elements generate a horse-shoe vortex and a pair of vortices in their wake. This is exactly the kind of disturbance that Tumin and Reshotko showed would lead to optimal transient growth. White et al.<sup>4,5,6</sup> have performed a series of experiments involving subsonic flow over an array of cylindrical roughness elements and have identified transient growth in the wake of the array. Fischer and Choudhari<sup>7</sup> and Choudhari and Fischer<sup>8</sup> performed numerical simulations of White's experiments. They also confirmed the presence of transient growth. Reshotko and Tumin<sup>9</sup> used their spatial transient growth theory to produce a model for roughness-induced transition. Their model reproduced the trends of Reda and the passive nosetip technology (PANT) data.<sup>10,11</sup>

Recent work has shifted to the possible existence of an absolute instability being generated by the roughness. For taller roughness elements in subsonic flow, the wake region is dominated by unsteady hairpin vortices.<sup>12</sup> Ergin and White<sup>13</sup> conducted experiments of unsteady low-speed flow over isolated roughness elements. They found the locations of maximum fluctuation intensity to correspond to locations of inflection points in the streamwise velocity. This suggests that the unsteadiness seen in subsonic flow may have been caused by a Kelvin-Helmholtz type instability. The unsteady vortex shedding seen in subsonic flow is not present in supersonic flow.<sup>14</sup> This difference may be due to the stabilizing effect of high Mach numbers on shear layers.<sup>15</sup> Although the unsteadiness is no longer present, a similar instability may still remain.

Danehy et al.<sup>16</sup> visualized Mach 4.2 flow over an isolated 2 mm radius hemispherical roughness element using Nitric oxide planar laser-induced fluorescence (PLIF). They showed that breakdown to turbulence begins in the downstream legs of the horse-shoe vortex that forms upstream of the roughness. Chang et al.<sup>17</sup> have recently performed numerical simulations that support these results. They found strong unsteadiness in Mach 4.16 flow over isolated cylindrical roughness elements with heights of 1.3 and 2.5 times the boundary-layer thickness with the unsteadiness first visible in the legs of the horse-shoe vortices. Spectral analysis and the computed evolution of disturbance root mean square amplitude suggest that the source for the unsteadiness is a possible absolute instability located in the separation region formed upstream of the roughness element. Bartkowicz et al.<sup>18</sup> have simulated flow inside the Boeing/AFOSR Mach 6 quiet wind tunnel at Purdue University with a cylindrical roughness element and reproduced an instability which was measured experimentally.<sup>19,20</sup> They suggest that the instability is created by an unsteady high-momentum jet created near the top of the roughness, which flows down into the vortex system located near the wall. Duan et al.<sup>21</sup> have also simulated flow under the conditions from the Purdue wind tunnel. They measured a different instability frequency than the experiments but this may have been due to discrepancies between the simulated geometry and the actual wind tunnel.

The objective of our work is to study the physical mechanisms behind transition in hypersonic boundary layers due to isolated surface roughness. This will be accomplished by numerically simulating flow with conditions similar to those of recent roughness experiments done in the Boeing/AFOSR Mach 6 quiet wind tunnel at Purdue University.<sup>19,20</sup> The compressible Navier-Stokes equations are solved on a Cartesian grid using a fifth-order hybrid WENO scheme combined with a third-order cut-cell<sup>22,23</sup> method to model the roughness. In our previous attempt at this simulation,<sup>23</sup> the runtime was too great to allow completion of the simulation. To alleviate this problem, a multi-zone refinement method was added to the code. The multi-zone refinement method provides more control over the grid point placement. This will reduce the required number of grid points and thus the simulation runtime. Two-dimensional and three-dimensional test cases for the combined cut-cell and multi-zone refinement method will be presented. Results will also be shown which confirm that the desired high-order of convergence is obtained. Preliminary results for the simulation of Mach 6 flow over the roughness element used at Purdue University will also be presented.

## II. Methodology

The governing equations in Cartesian coordinates,  $(x_1, x_2, x_3) = (x, y, z)$ , are the three-dimensional unsteady compressible Navier-Stokes equations for a calorically perfect gas with density  $\rho$ , pressure  $p$ , tem-

perature  $T$ , and velocity  $(u_1, u_2, u_3) = (u, v, w)$ :

$$\frac{\partial \hat{\mathbf{U}}}{\partial t} + \frac{\partial \hat{\mathbf{F}}_j}{\partial x_j} = \frac{\partial \hat{\mathbf{F}}_{v,j}}{\partial x_j}, \quad j = 1, 2, 3 \quad (1)$$

where  $\hat{\mathbf{U}}$  is the vector of conservative variables,  $[\rho, \rho u, \rho v, \rho w, E]^T$ .  $\hat{\mathbf{F}}_j$  and  $\hat{\mathbf{F}}_{v,j}$  are the vectors of the inviscid and viscous fluxes, respectively, in the  $j$ th direction and are given as

$$\hat{\mathbf{F}}_j = \begin{pmatrix} \rho u_j \\ \rho u_1 u_j + \delta_{1j} p \\ \rho u_2 u_j + \delta_{2j} p \\ \rho u_3 u_j + \delta_{3j} p \\ u_j (E + p) \end{pmatrix}, \quad \text{and} \quad \hat{\mathbf{F}}_{v,j} = \begin{pmatrix} 0 \\ \tau_{1j} \\ \tau_{2j} \\ \tau_{3j} \\ u_k \tau_{kj} - q_j \end{pmatrix}. \quad (2)$$

The total energy per unit mass  $E$ , the viscous stress tensor  $\tau_{ij}$ , and the heat flux vector  $q_j$  are defined as

$$E = \frac{p}{\gamma - 1} + \frac{1}{2} \rho u_i u_i, \quad (3)$$

$$\tau_{ij} = \mu \left( \frac{\partial u_i}{\partial x_j} + \frac{\partial u_j}{\partial x_i} - \frac{2}{3} \delta_{ij} \frac{\partial u_k}{\partial x_k} \right), \quad (4)$$

$$q_j = -k \frac{\partial T}{\partial x_j}, \quad (5)$$

where  $\mu$  is the fluid viscosity and  $k$  is the thermal conductivity. The system of equations is closed by the equation of state. Since the gas is calorically perfect, the equation of state is

$$p = \rho R T. \quad (6)$$

The gas is assumed to be air so the gas constant,  $R$ , has a value of  $287.04 \text{ m}^2/\text{s}^2 \text{ K}$ , the ratio of the specific heats,  $\gamma$ , is 1.4 and the Prandtl number,  $Pr$ , is 0.72. The viscosity is computed using Sutherland's law in the form

$$\mu = \mu_r \left( \frac{T}{T_r} \right)^{1.5} \frac{T_r + T_s}{T + T_s} \quad (7)$$

where  $\mu_r = 1.7894 \times 10^{-5} \text{ (N s)/m}^2$ ,  $T_s = 110.33 \text{ K}$ , and  $T_r = 288 \text{ K}$ . All variables are left in dimensional form.

The flow fields are obtained through direct numerical simulation of the governing equations. Before solving, the governing equations are transformed from the physical  $(x, y, z)$  space to a  $(\xi, \eta, \zeta) = (\xi^1, \xi^2, \xi^3)$  computational space. The grid in the computational space is uniformly spaced in  $\xi$ ,  $\eta$ , and  $\zeta$  with each varying from 0 to 1. After the transformation, the governing equations become

$$\frac{\partial \mathbf{U}}{\partial t} + \frac{\partial \mathbf{F}_j}{\partial \xi^j} = \frac{\partial \mathbf{F}_{v,j}}{\partial \xi^j}, \quad j = 1, 2, 3 \quad (8)$$

where  $\mathbf{U}$  is a vector of the conservative variables,  $[\rho, \rho u, \rho v, \rho w, E]^T / J$ .  $J$  is the determinant of the Jacobian matrix:

$$J = \left| \frac{\partial (\xi, \eta, \zeta)}{\partial (x, y, z)} \right| \quad (9)$$

$\mathbf{F}_j$  and  $\mathbf{F}_{v,j}$  are the vectors of the inviscid and viscous fluxes, respectively, in the  $j$ th direction of the computational space and are given as

$$\mathbf{F}_j = \frac{1}{J} \begin{pmatrix} \rho U_j \\ \rho u_1 U_j + \delta_{1j} \xi_1^j p \\ \rho u_2 U_j + \delta_{2j} \xi_2^j p \\ \rho u_3 U_j + \delta_{3j} \xi_3^j p \\ U_j (E + p) \end{pmatrix}, \quad \text{and} \quad \mathbf{F}_{v,j} = \frac{1}{J} \begin{pmatrix} 0 \\ \xi_k^j \tau_{1k} \\ \xi_k^j \tau_{2k} \\ \xi_k^j \tau_{3k} \\ \xi_k^j u_n \tau_{nk} - \xi_k^j q_k \end{pmatrix} \quad (10)$$

where  $\xi_k^j \equiv \frac{\partial \xi^j}{\partial x_k}$  are the metrics and  $U_j$  is given by

$$U_j = u_k \xi_k^j. \quad (11)$$

The shear stresses and heat fluxes in curvilinear coordinates are

$$\tau_{ij} = \mu \left( \xi_j^k \frac{\partial u_i}{\partial \xi^k} + \xi_i^k \frac{\partial u_j}{\partial \xi^k} - \frac{2}{3} \delta_{ij} \xi_k^n \frac{\partial u_k}{\partial \xi^n} \right), \quad (12)$$

$$q_j = -k \xi_j^k \frac{\partial T}{\partial \xi^k}. \quad (13)$$

The inviscid terms in the governing equation are split using local Lax-Friedrichs flux splitting for upwinding.

$$\mathbf{F}_j = \mathbf{F}_j^+ + \mathbf{F}_j^- \quad (14)$$

where  $\mathbf{F}_j^\pm$  is

$$\mathbf{F}_j^\pm = \frac{1}{2} (\mathbf{F}_j \pm \lambda_j \mathbf{U}) \quad (15)$$

and  $\lambda_j$  is

$$\lambda_j = \sqrt{(u_k \xi_k^j)^2 + \epsilon^2 c^2 \left( (\xi_1^j)^2 + (\xi_2^j)^2 + (\xi_3^j)^2 \right)} + c \sqrt{(\xi_1^j)^2 + (\xi_2^j)^2 + (\xi_3^j)^2} \quad (16)$$

where  $c$  is the speed of sound and  $\epsilon$  is 0.1.

The inviscid terms are computed using a fifth-order finite-difference hybrid WENO scheme. The scheme begins by writing the derivatives in conservative form. As an example, the derivative of the inviscid flux in the  $\xi$  direction with respect to  $\xi$  at point  $i$  is computed as

$$\frac{\partial \mathbf{F}_\xi}{\partial \xi}(\xi_i) = \frac{\mathbf{F}_\xi^+(\xi_{i+1/2}) - \mathbf{F}_\xi^+(\xi_{i-1/2})}{\Delta \xi} + \frac{\mathbf{F}_\xi^-(\xi_{i+1/2}) - \mathbf{F}_\xi^-(\xi_{i-1/2})}{\Delta \xi}. \quad (17)$$

The interface flux is a linear combination of a fifth-order WENO scheme and a fifth-order low-dissipation scheme. For the positive eigenvalue fluxes, the interface flux would be

$$\mathbf{F}_\xi^+(\xi_{i+1/2}) = (1 - \sigma) \mathbf{F}_\xi^{+\text{WENO}}(\xi_{i+1/2}) + \sigma \mathbf{F}_\xi^{+\text{LD}}(\xi_{i+1/2}) \quad (18)$$

where  $\sigma$  is the hybrid switch and comes from Ren et al.<sup>24</sup> The WENO flux is computed using the mapped WENO scheme of Hendrick et al.<sup>25</sup> However, instead of computing the WENO weights for each of the individual fluxes, the weights are just computed from the fluid density. The low-dissipation flux is computed using a conservative version of the fifth-order scheme of Zhong.<sup>26</sup> The low-dissipation flux is computed as

$$\mathbf{F}_\xi^{+\text{LD}}(\xi_{i+1/2}) = \sum_{j=-2}^3 a_j \mathbf{F}_\xi^+(\xi_{i+j}) \quad (19)$$

where the constants  $a_j$  are

$$a_{-2} = 1 - \frac{1}{12} \alpha \quad (20)$$

$$a_{-1} = -8 + \frac{5}{12} \alpha \quad (21)$$

$$a_0 = 37 - \frac{5}{6} \alpha \quad (22)$$

$$a_1 = 37 + \frac{5}{6} \alpha \quad (23)$$

$$a_2 = -8 - \frac{5}{12} \alpha \quad (24)$$

$$a_3 = 1 + \frac{1}{12} \alpha \quad (25)$$

$$(26)$$

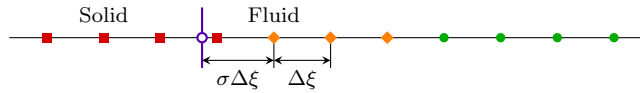


Figure 1. Cut-cell point classification for sample  $\xi$  grid line. Immersed boundary —; boundary point  $\circ$ ; points using interior scheme  $\bullet$ ; points using a non-uniform one-sided stencil  $\blacklozenge$ ; points not used in simulation  $\blacksquare$ .

The constants for the negative eigenvalue fluxes can be found from symmetry. The  $\alpha$  in the constants controls the scheme's dissipation and stability and is equivalent to the  $\alpha$  from Zhong.<sup>26</sup> In this work,  $\alpha$  was set to -6. A third-order TVD<sup>27</sup> scheme was used for time advancement and the viscous terms were computed using sixth-order central finite difference scheme.

## II.A. Cut-Cell Method

The cut-cell method used in this work was originally developed by Duan et al.<sup>22</sup> The current work used a modified version, which was presented in Greene et al.<sup>23</sup> The cut-cell method is a third-order method for simulating flows on grids with non-body-conforming geometries. When the cut-cell method is combined with our interior scheme, the global order of convergence will be fourth order. The method allows numerical simulations of flow over an arbitrary geometry to be performed on simple Cartesian grids.

The main idea behind the cut-cell method is to switch to a non-uniform one-sided finite-difference stencil whenever the normally used stencil would cross the immersed boundary. Figure 1 shows a sample  $\xi$  direction grid line for the cut-cell method. The boundary of an immersed object cuts across the grid line with the solid on the left and the fluid on the right. None of the points within an immersed boundary are used in the simulation. In addition, any points deemed too close to the boundary are not included either. The first fluid point to the right of the immersed boundary is such a point. If the interior scheme was used at the next three points away from the boundary, their stencils would include points within the solid. Instead of using the interior scheme, those points utilize a non-uniform one-sided stencil. The stencils are non-uniform because they can include the boundary point values. The remaining fluid points use the uniform stencil of the interior scheme.

## II.B. Multi-Zone Refinement Method

The multi-zone refinement method utilizes overlapping grids to precisely control grid resolution. The method used in this work comes from Shen et al.<sup>28</sup> Shen et al. developed a high-order finite-difference WENO version of the adaptive mesh refinement method. Since their method was adaptive, the refinement zones would move with the flow physics. In our work, the locations needing increased resolution are fixed in time. Therefore, a stationary refinement grid version was used in this work.

Figure 2 depicts the process for adding a one-dimensional refinement grid. The method begins by placing a single coarse grid over the entire flow field. Figure 2(a) shows the coarse grid at the  $t^n$  and  $t^{n+1}$  time steps. Next smaller grids with increased resolution are placed on top of the coarse grid in locations where complex physics are expected. Figure 2(b) shows a refinement grid with a factor of three increase in resolution placed over the coarse grid. Six ghost points are attached to the edge of the refinement grid. The flow variables at the ghost points are computed from the coarse grid using fifth-order interpolation. Most of the coarse grid points which are overlapped by refinement grid points become coarse grid ghost points. The flow variables at these points are simply set equal to the corresponding refinement grid point values. In addition to the spatial refinement, the temporal resolution of the refinement grid is also increased by the same factor. Figure 2(c) shows the additional time steps taken by the refinement grid. The flow variables at the refinement grid ghost points for the additional time steps are computed from the ghost points at steps  $t^n$  and  $t^{n+1}$  using fourth-order Hermite interpolation. This requires that the coarse grid be advanced in time before advancing the refinement grid since coarse grid values at  $t^n$  and  $t^{n+1}$  are required to compute the refinement grid ghost points.

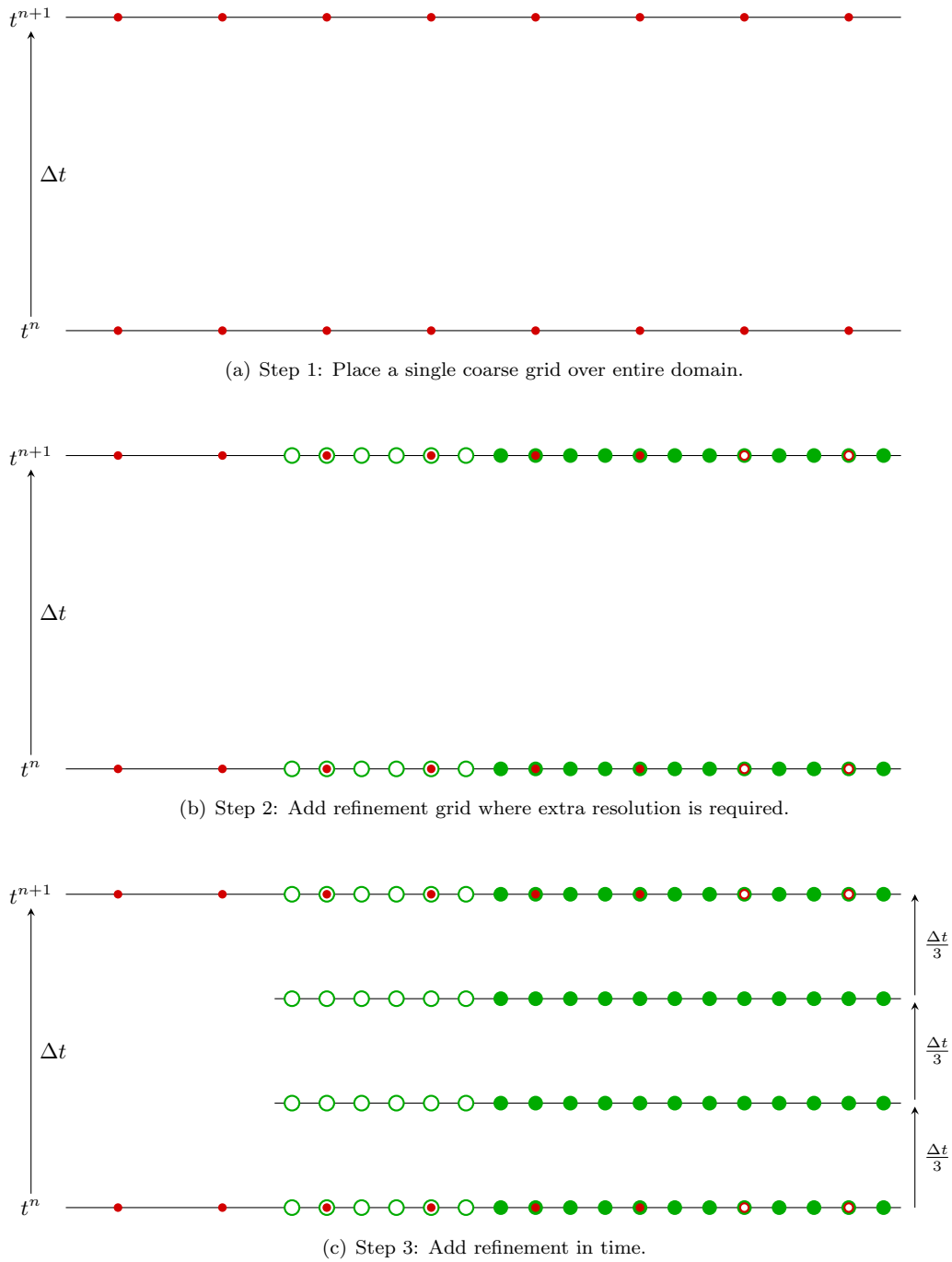
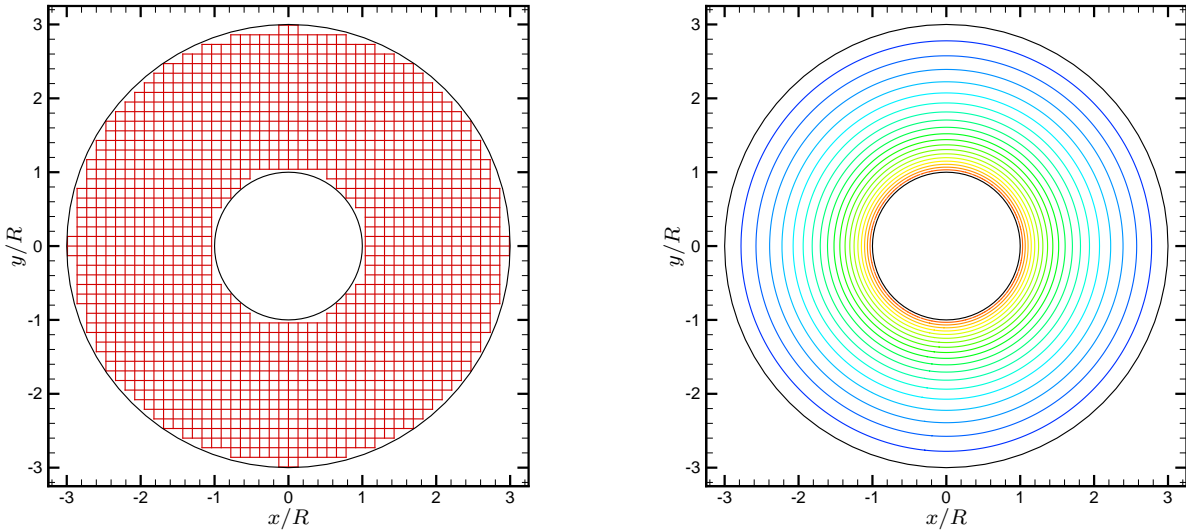


**Figure 2. Multi-zone refinement grid generation and point classification. Coarse grid point ●; coarse grid ghost point ○; refinement grid point ●; refinement grid ghost point ○.**



(a) Sample grid with  $50 \times 50$  points. Points inside the cylinders are not shown.

(b) Mach number contour from  $200 \times 200$  grid. 21 evenly spaced levels from 0.0 to 1.0.

Figure 3. Sample grid and Mach number contour for circular Couette flow test case.

### III. Order of Convergence

The order of convergence was computed to ensure that the target high-order of convergence was achieved. Two test cases were used to find the order of convergence. The simulations tested the cut-cell and mesh refinement methods individually.

#### III.A. Cut-cell Method Order of Convergence

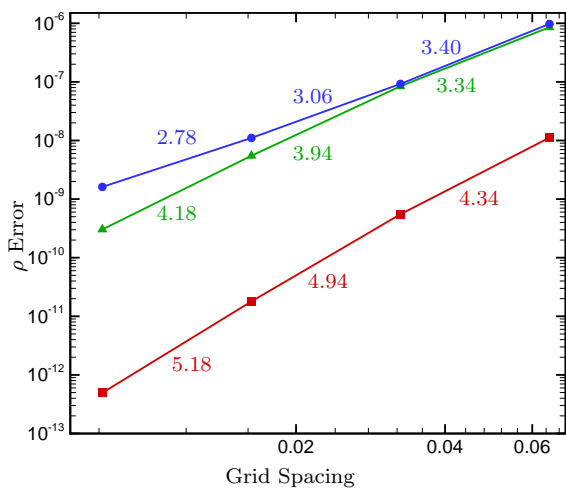
The order of convergence for the cut-cell cell portion of the code was tested using circular Couette flow. The problem consists of two concentric cylinders with a viscous fluid between them. For our test case, the gap between the cylinders is twice the inner cylinder radius ( $R$ ). The inner cylinder rotated with a Mach number of one while the outer cylinder was stationary. Both walls were isothermal. The inner cylinder was set to a temperature of 300 K and the outer cylinder was set to 400 K. The Reynolds number based on the inner cylinder radius is 500. The simulation was performed assuming a constant viscosity. This permitted the comparison to an analytical exact solution.

The simulation was performed on a uniform Cartesian grid measuring  $6.5R \times 6.5R$ . Both cylinders were imposed by the cut-cell method. Figure 3(a) shows a sample of the grid using  $50 \times 50$  grid points. The simulation was carried out on four grids:  $100 \times 100$ ,  $200 \times 200$ ,  $400 \times 400$ , and  $800 \times 800$ . Figure 3(b) shows the Mach contours for the solution computed on the  $200 \times 200$  grid. Despite being simulated on a Cartesian grid, the contours are circular as the exact solution predicts.

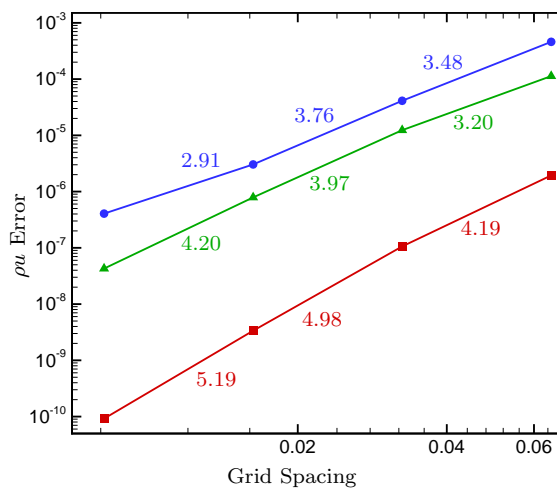
Figure 4 shows the  $L^2$ ,  $L^1$ , and  $L^\infty$  errors for the conservative variables from each of the grid resolutions. The number next to each line segment is the slope of that segment which is equal to the order of convergence. The cut-cell method uses third-order differencing near the immersed surface. When combined with the fifth-order interior scheme, the expected global order of convergence is four. The  $L^1$  error shows that the order of convergence is near the desired value of four.

#### III.B. Multi-Zone Refinement Method Order of Convergence

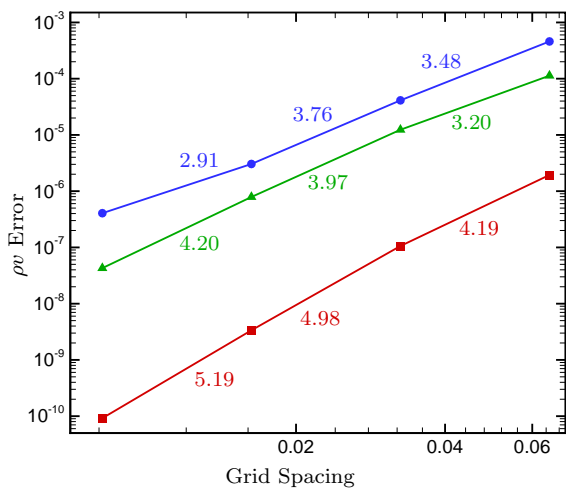
The order of convergence for the multi-zone refinement portion of the code was tested by simulating the propagation of a low-amplitude density wave. The wave was sinusoidal in shape with an amplitude of 10% of the mean density. The wave propagates at an angle of approximately  $26^\circ$  with the  $x$  axis. The viscous terms were turned off for this simulation.



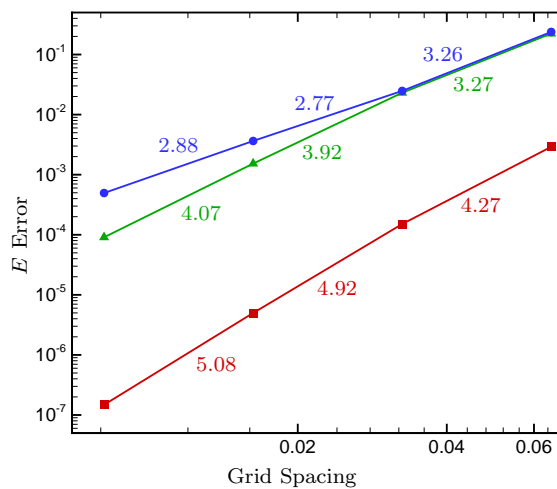
(a) Error in density.



(b) Error in  $x$ -direction momentum.



(c) Error in  $y$ -direction momentum.



(d) Error in energy.

Figure 4. Error in the conservative variables versus grid spacing for the circular Couette flow test case. The number next to each line segment is the order of convergence computed using the line segment end points.  $L^\infty$  error —●—;  $L^1$  error —▲—;  $L^2$  error —■—.

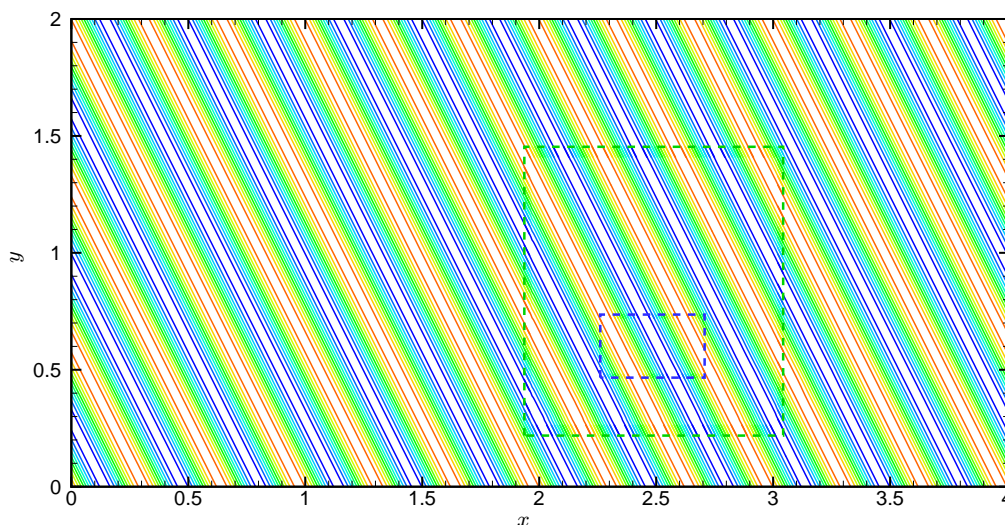


Figure 5. Density contour for propagating density wave problem at a final time of 2.0. The dashed green box represents the first refinement zone which increases the resolution by a factor of three compared to the coarse grid. The dashed blue box represents the second refinement zone which increases the resolution by a factor of three compared to the first refinement grid.

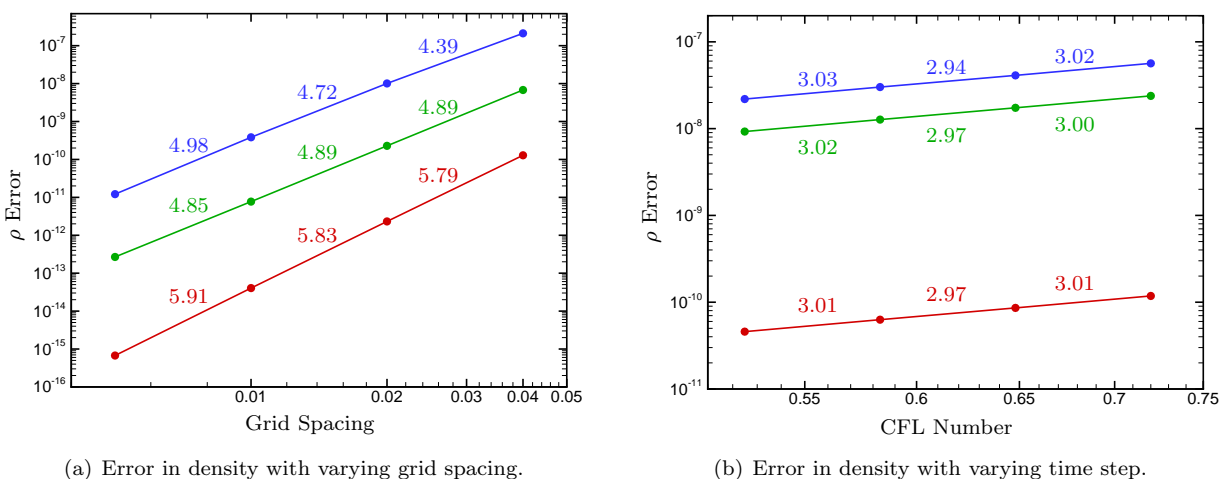


Figure 6. Error in density for density wave test case. The number next to each line segment is the order of convergence computed using the line segment end points.  $L^\infty$  error — blue;  $L^1$  error — green;  $L^2$  error — red.

Figure 5 shows the density contour for the simulation at a final time of 2.0. The figure also shows the locations of the first and second refinement zones. The first zone increases the resolution by a factor of three compared to the coarse grid and the second increases the resolution by another factor of three. Periodic boundary conditions are used along the coarse grid edges.

The simulation was performed on a uniform Cartesian grid. In order to compute the spatial and temporal order of convergence, two sets of simulations were performed. In the first, the CFL number was fixed at 0.1 while the number of grid points was changed. Four simulations were carried out with the coarse grid having  $100 \times 50$ ,  $200 \times 100$ ,  $400 \times 200$ , and  $800 \times 400$  points. The results from this set of simulations were used to compute the spatial order of convergence. Figure 6(a) shows the  $L^2$ ,  $L^1$ , and  $L^\infty$  errors for density from each of the grid resolutions. Since the cut-cell method is not used in this case and the domain is periodic, the optimal order of the interior scheme should be obtained. Since a fifth-order hybrid scheme is being used, the expected order of convergence is five. As the  $L^1$  error shows, the desired value of five is obtained.

In the second set of simulations, the grid was kept constant while the CFL number was changed. Four simulations were performed with a CFL number of 0.8, 0.72, 0.648, 0.5832, and 0.52488. The results from this set of simulations was used to compute the temporal order of convergence. Figure 6(b) shows the  $L^2$ ,

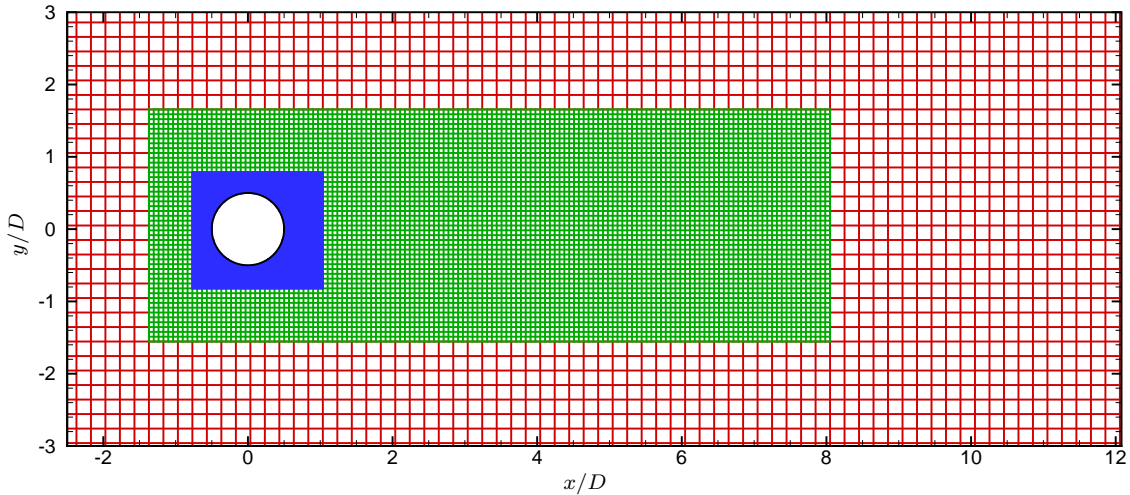


Figure 7. Grid in vicinity of cylinder. Points inside the cylinder are not shown. Coarse grid shown in red. First refinement grid with three times the resolution shown in green. Second refinement grid with an additional three times increase in resolution shown in blue. Only every second point shown in both directions.

$L^1$ , and  $L^\infty$  errors for density from each of the CFL values. Since a third-order Runge-Kutta scheme is used to advance the simulation in time and the multi-zone refinement uses a fourth-order Hermite interpolation in time, the expected temporal order of convergence is three. All three errors show the expected order of convergence.

## IV. Results

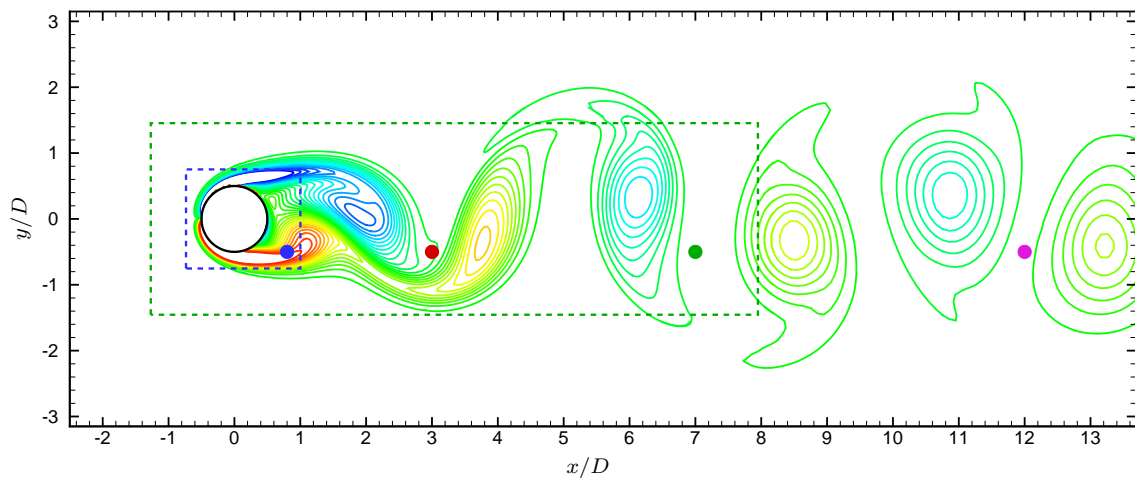
### IV.A. Subsonic Flow Over Cylinder

The first set of results being presented is for Mach 0.2 flow over a cylinder. The purpose of this simulation was to test the combination of the cut-cell and multi-zone methods on an unsteady problem. Although the code solves the compressible Navier-Stokes equations, this incompressible problem was selected due to its widely known solution. The Reynolds number for the flow based on the cylinder diameter ( $D$ ) is 150. This places the solution in the periodic vortex shedding regime.

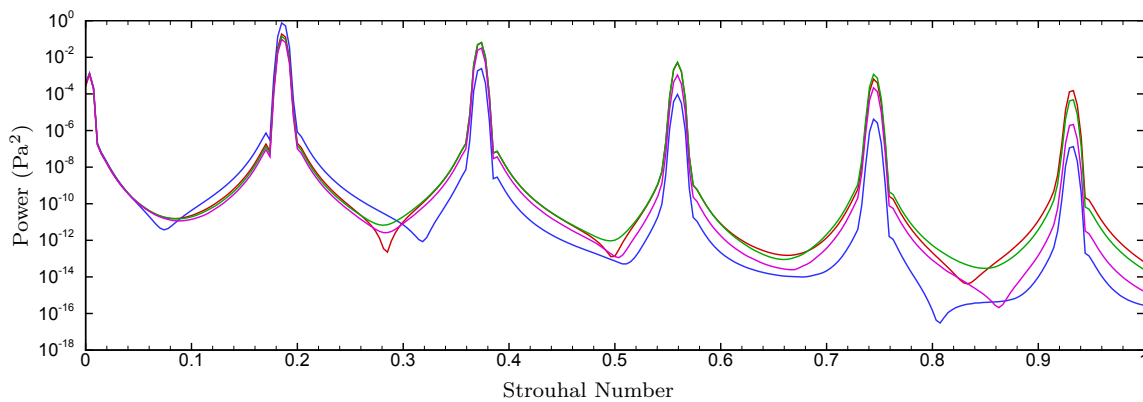
Figure 7 shows the grids used in the simulation. The red grid is the coarse grid, which covers the entire domain. The coarse grid has 300 grid points in the  $x$  direction and 150 grid points in the  $y$  direction. The first refinement grid is shown in green and second in blue. Each refinement grid increases the resolution by a factor of three. The figure only shows a portion of the domain. In the  $x$  direction, the domain starts at  $x/D = -5$  and ends at  $x/D = 15$ . The domain has a length of  $10D$  in the  $y$  direction and is centered at  $y/D = 0$ . Non-reflective boundary conditions<sup>29</sup> are used along all edges of the domain.

Figure 8(a) shows contours of vorticity for the flow after reaching a periodic state. The green and blue boxes show the location of the first and second refinement grid, respectively. The results show that the vortices are able to pass across the refinement zone boundaries unimpeded. Figure 8(a) also shows the location of four probes placed in the flow. Once the solution reached a periodic state, the pressure at each probe location was recorded as a function of time. The dominant frequency of the pressure history was computed using an FFT. The results of the FFT are shown in Figure 8(b). The different line colors correspond to the same colored probe in Figure 8(a). Figure 8(b) shows that all the probes measured the same dominant frequency. This suggests that the multi-zone refinement did not have a noticeable negative effect on the solution. The first peak measured by all the probes is at a Strouhal number of 0.185. The remaining peaks are harmonics of the first.

Figure 9 is a plot taken from the cylinder wake review paper by Williamson.<sup>30</sup> The plot shows the Strouhal number versus Reynolds number for the current problem. The data comes from a number of different experiments. The Strouhal number from the current simulation was added to the plot. The results agree very well with the experimental data. These results suggest that the cut-cell method and the multi-zone refinement are working correctly.



(a) Vorticity contour. Colored dots denote the location of pressure probes. First refinement zone edge - - -. Second refinement zone edge - - -.



(b) FFT of the pressure history record at each probe. The line color corresponds to the probe color in Figure (a).

**Figure 8. Results from subsonic flow over a cylinder.**

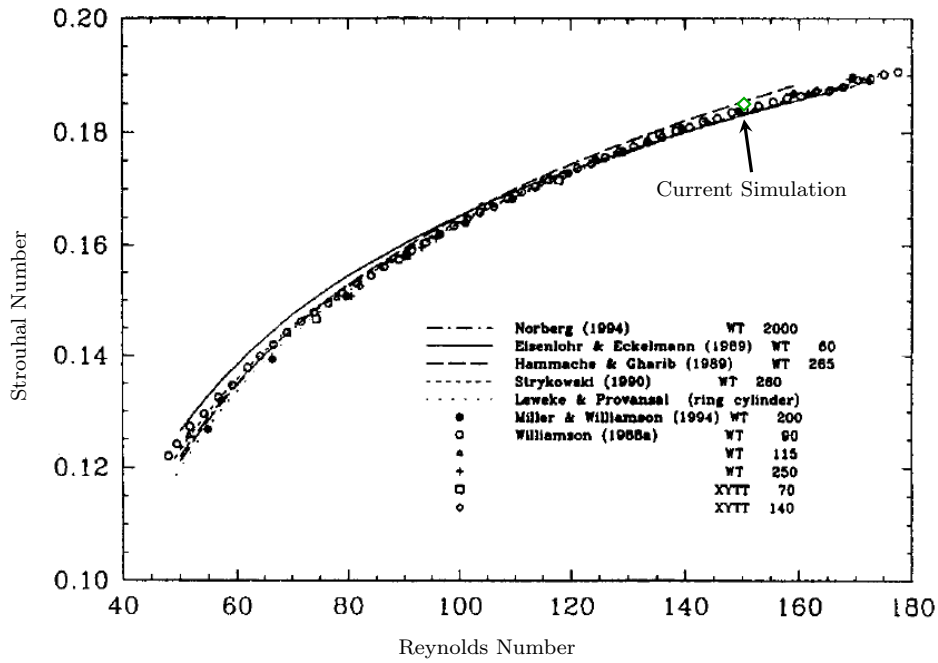


Figure 9. Strouhal number versus Reynolds number for incompressible flow over a cylinder. Taken from Williamson.<sup>30</sup> Results from current simulation shown as  $\diamond$ .

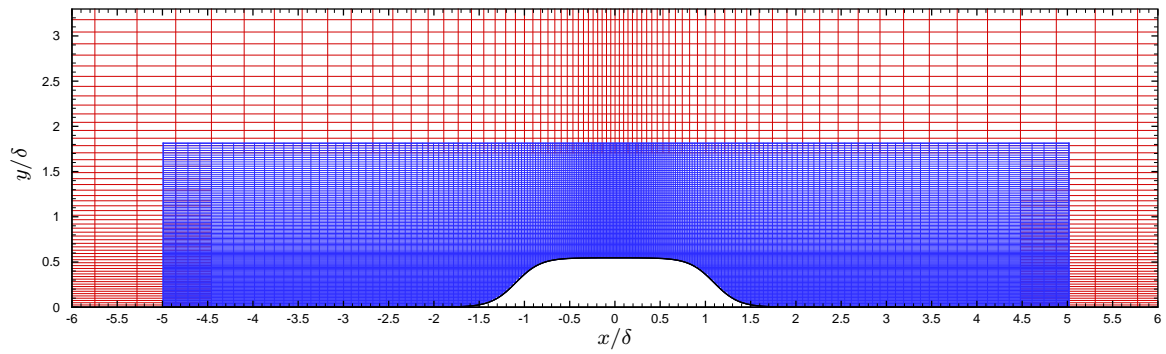
Freestream Mach number	$M_\infty$	4.8
Freestream velocity	$u_\infty$	720 m/s
Freestream pressure	$p_\infty$	239.426 Pa
Freestream temperature	$T_\infty$	55.4 K
Freestream density	$\rho_\infty$	$1.51 \times 10^{-2}$ kg/m <sup>3</sup>
Freestream Reynolds number	$Re_\infty$	$10^5$
Reference length	$L_{ref}$	$3.365 \times 10^{-2}$ m
Roughness height	$k$	$0.1L_{ref}$
Ratio of roughness height to boundary-layer thickness	$k/\delta$	0.547

Table 1. Flow conditions for the hyperbolic tangent roughness simulation.

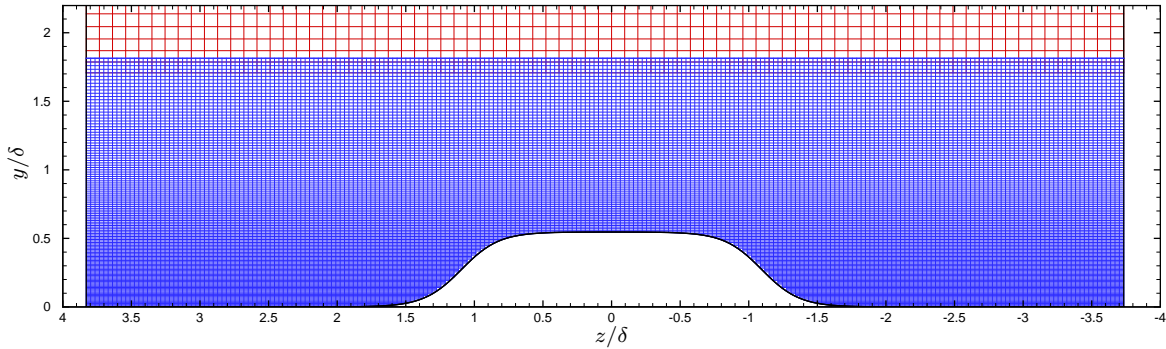
#### IV.B. Hyperbolic Tangent Roughness

This simulation comes from Marxen and Iaccarino.<sup>31</sup> Marxen and Iaccarino simulated Mach 4.8 boundary-layer flow over a three-dimensional isolated roughness constructed from hyperbolic tangent curves located on a flat plate. The roughness height to undisturbed boundary-layer thickness ratio ( $k/\delta$ ) is 0.547. The freestream conditions for the flow are summarized in Table 1, where  $Re_\infty = \rho_\infty u_\infty L_{ref} / \mu_\infty$  and  $\delta$  is the boundary-layer thickness of the flow without the roughness element. The equation for the roughness geometry can be found in Marxen and Iaccarino. This roughness was previously simulated using a single body-fitted grid and a single cut-cell grid in Greene et al.<sup>23</sup> The simulation was recomputed using the multi-zone refinement method. The new simulation used a coarse grid and one refinement grid. The purpose of the simulation was to test the multi-zone method on a compressible problem and find the runtime reduction the method provides.

The grids in the vicinity of the roughness are shown in Figure 10. The coarse grid has 120 points in the  $x$  direction, 80 points in the  $y$  direction, and 80 points in the  $z$  direction. The refinement grid increases the resolution by a factor of three. The grids are clustered near the roughness element in the  $x$  direction and near the wall in the  $y$  direction. The grid is uniform in the  $z$  direction. Only the domain around the roughness element is shown in the figure. The full numerical domain starts at  $x/\delta = -24.0$  and ends at  $x/\delta = 72.0$ . The top of the domain is located at  $y/\delta = 8.6$  and the domain half width is  $W/\delta = 3.8$ .

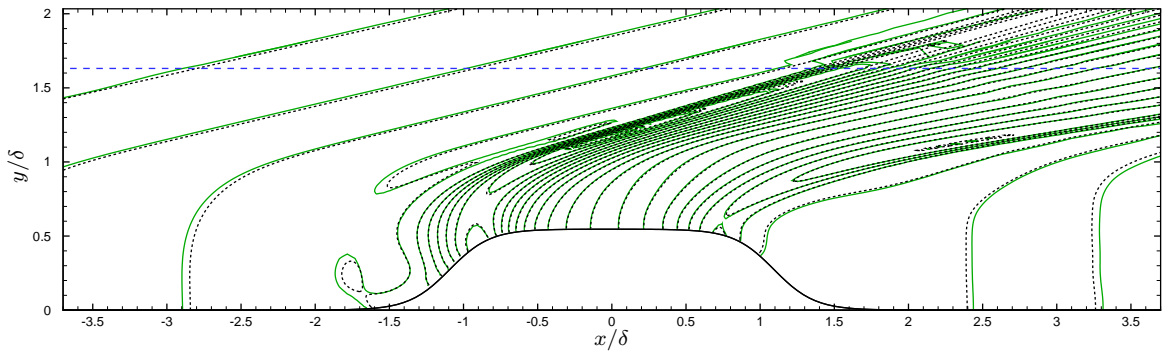


(a)  $x - y$  plane at  $z/\delta = 0$

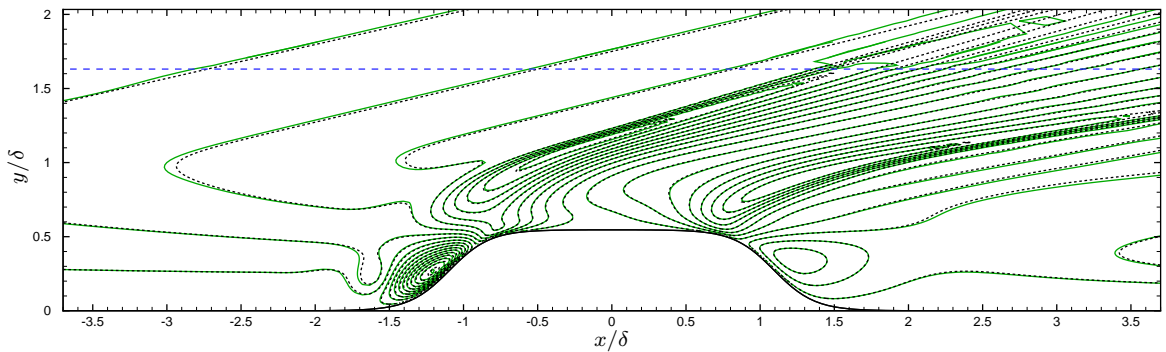


(b)  $y - z$  plane at  $x/\delta = 0$

**Figure 10.** Grid in the vicinity of the three-dimensional hyperbolic tangent roughness element. Grid points inside the roughness were removed. Coarse grid shown in red. Refinement grid with three times the resolution shown in blue.

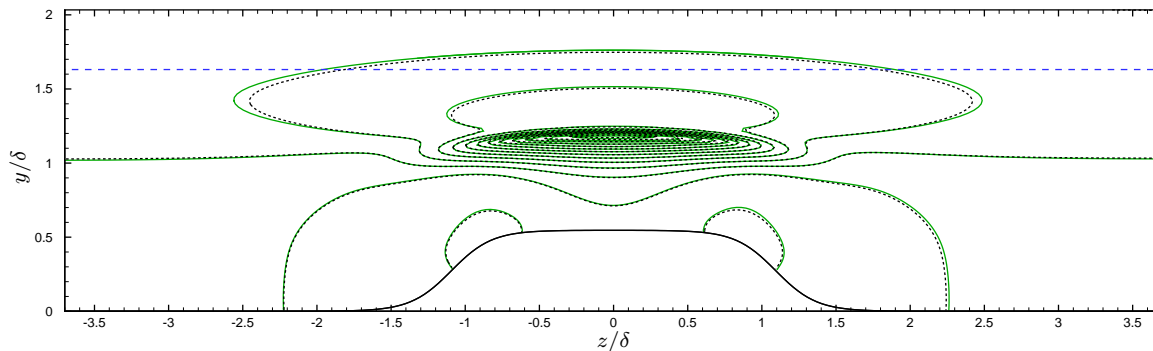


(a) Pressure contour. Non-dimensionalized as  $p/p_\infty$ . 32 levels from 0.05 to 1.6.

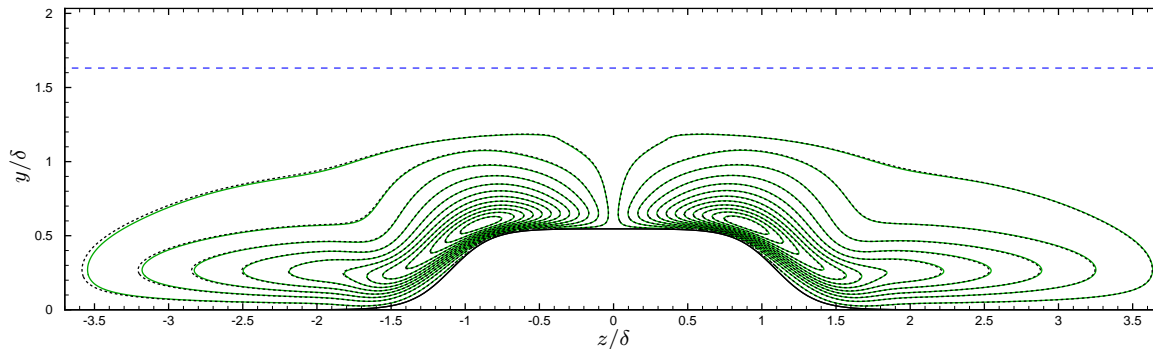


(b)  $v$  velocity contour. Non-dimensionalized as  $v/u_\infty$ . 24 levels from -0.1 to 0.1.

**Figure 11.** Contours in vicinity of three-dimensional hyperbolic tangent roughness element at  $z/\delta = 0$  plane. Multi-zone cut-cell simulation —; Body-fitted simulation - - -; Refinement zone edge - - -.



(a) Pressure contour. Non-dimensionalized as  $p/p_\infty$ . 32 levels from 0.1 to 1.6.



(b)  $w$  velocity contour. Non-dimensionalized as  $w/u_\infty$ . 24 levels from -0.1 to 0.1.

**Figure 12.** Contours in vicinity of three-dimensional hyperbolic tangent roughness element at  $x/\delta = 0$  plane. Multi-zone cut-cell simulation —; Body-fitted simulation - - -; Refinement zone edge - - -.

The leading edge of the flat plate is not included in the simulation. Instead, a compressible similarity solution is imposed at the inlet of the numerical domain and held fixed with time. The outlet of the domain is a supersonic outlet so the conservative variables are extrapolated from the interior of the domain. At the top of the domain, a sponge layer<sup>32</sup> is used to prevent the shock and expansion fan created by the roughness from reflecting back into the domain. The bottom edge of the domain is a no-slip adiabatic wall with the pressure being extrapolated from the domain interior. Symmetry boundary conditions are used at both edges on the domain in the  $z$  direction.

To evaluate the performance of the multi-zone refinement method, the results of the simulation were compared to the body-fitted results from Greene et al.<sup>23</sup> Contours of the pressure and the  $v$  velocity component near the roughness at the  $z/\delta = 0$  plane are shown in Figure 11. Contours of the pressure and the  $w$  velocity component near the roughness at the  $x/\delta = 0$  plane are shown in Figure 12. The results from the two methods agree very well. Only small differences between the body-fitted and current results are visible. Neither set of results were confirmed to be grid converged. Increasing the grid resolution may remove the differences. The multi-zone method provided a 75% reduction in runtime compare to the single grid methods used previously.

#### IV.C. Supersonic Flow Over The Ubuntu Logo

The test cases presented so far contained rather simple geometries. To test the code on a more complex geometry, supersonic flow over the logo of the Ubuntu<sup>33</sup> Linux distribution was simulated. The Ubuntu logo is shown in Figure 13. The freestream flow was set to Mach 3 with a Reynolds number based on the outer diameter of the logo's ring ( $D$ ) of 2,500 and a temperature of 100 K.

Figure 14 shows the grid used in the simulation. Only the grid near the logo is shown. The full domain goes from  $x/D = -5$  to  $x/D = 20$  in the  $x$  direction and  $y/D = -7.5$  to  $y/D = 7.5$  in the  $y$  direction. The coarse grid has 150 points in the  $x$  direction and 100 points in the  $y$  direction. Two refinement grids were used in the simulation. Each refinement grid increases the resolution by a factor of three. The grid is clustered near the center of the logo in both the  $x$  and  $y$  directions.



Figure 13. Logo for the Ubuntu<sup>33</sup> Linux distribution.

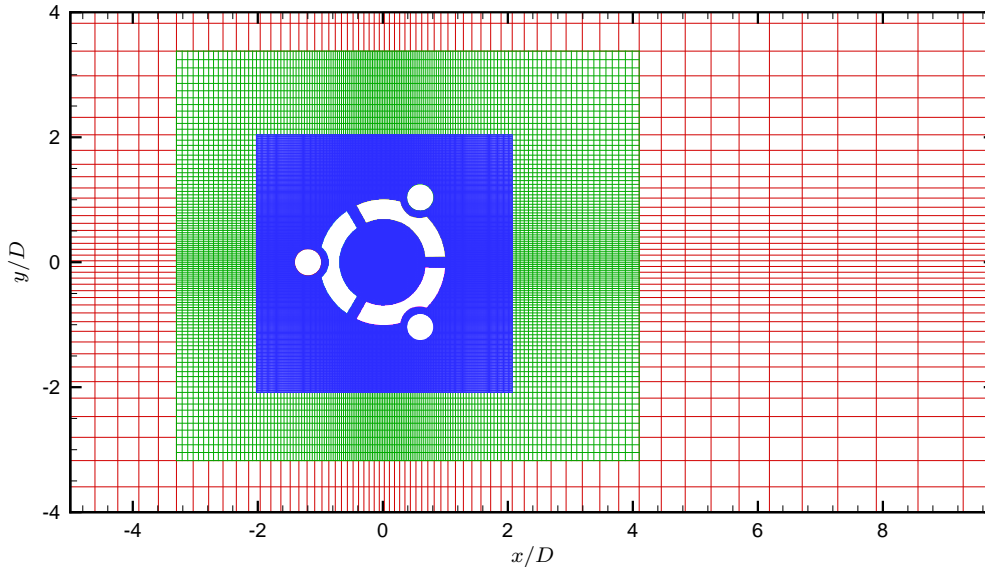


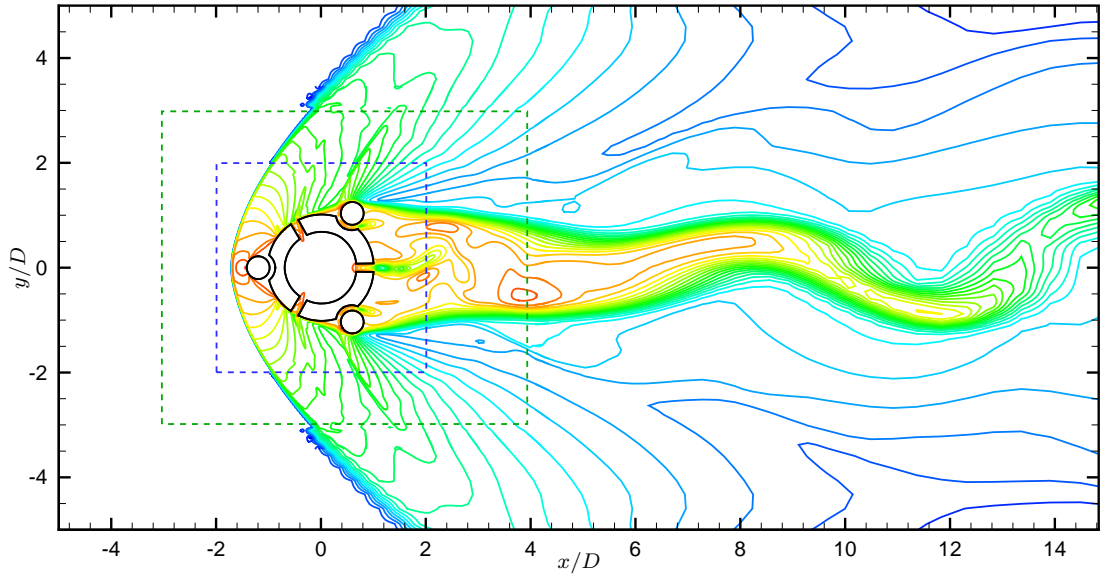
Figure 14. Grid near the Ubuntu logo. Points inside the logo are not shown. Coarse grid shown in red. First refinement grid with three times the resolution shown in green. Second refinement grid with an additional three times increase in resolution shown in blue. Only every second point shown in both directions.

Since the flow is supersonic, the freestream conditions are imposed at the inlet of the domain and help constant with time. The outlet is supersonic so the conservative variables are extrapolated from the interior of the domain. Sponge layers are placed at the top and bottom of the domain to prevent any shocks from reflecting back into the domain. The logo has no-slip adiabatic walls.

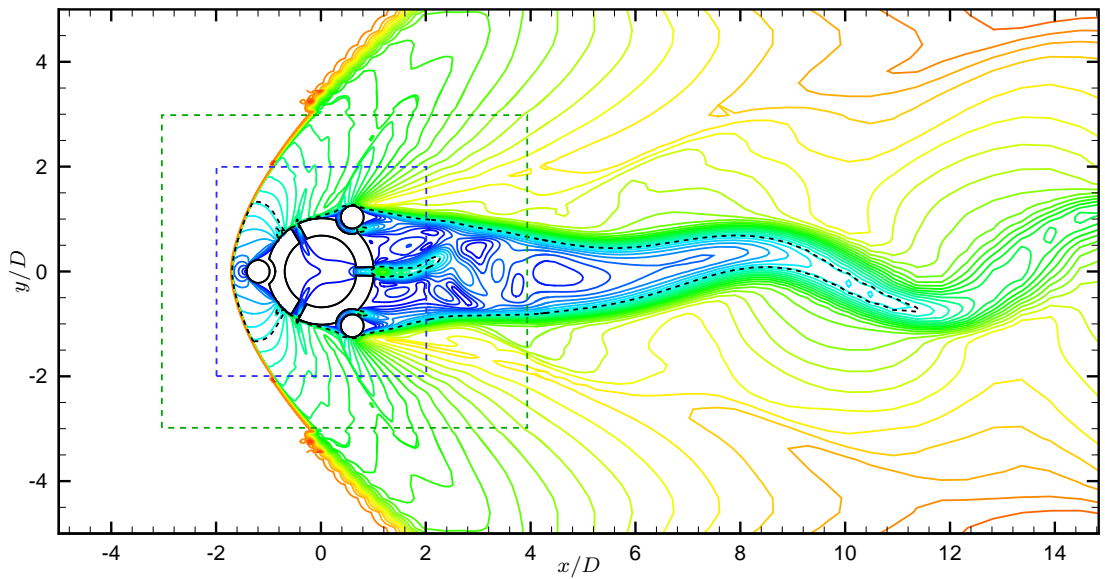
Contours of temperature and Mach number are shown in Figure 15. The dominant features of the flow are the bow shock created upstream of the logo and the unsteady wake. The results shown in the figure have reached a periodic state. The figure also demonstrates one of the weaknesses of the current multi-zone method. As the shock passes across a refinement grid boundary, the thickness of the shock increases abruptly. A weak reflected shock can sometimes also be propagated back into the refinement grid. The difference in the shock width and the strength of the reflected shock appears to be proportional to the strength of the shock. In the other simulations presented here, any shocks crossing a refinement boundary are significantly weaker and therefore do not create any issues.

Figure 16 shows contours of temperature and Mach number in the vicinity of the logo. The figure also includes a plot of the streamlines. Although there are no results to compare with for this flow, nothing stands out as incorrect in the flow field. This suggests the code is capable of handling complex geometries.

Once the solution reached a periodic state, the pressure was recorded at five locations in the flow. Figure 17(a) shows contours of vorticity and the location of the five pressure probes as colored dots. An FFT was used to compute the dominant frequency in the flow. Figure 17(b) shows the results of the FFT. The different line colors correspond to the same colored probe in the Figure 17(a). The same dominant frequency is measured by all the probes. The first peak is at a Strouhal number of 0.119. The remaining

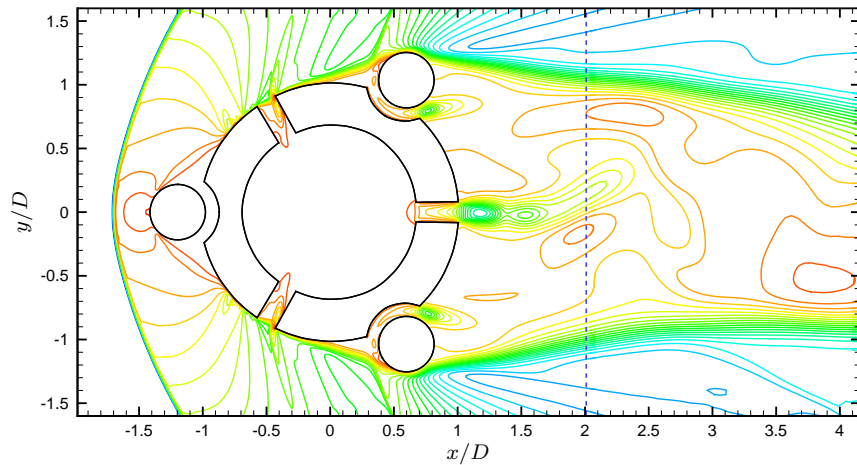


(a) Temperature contour. Non-dimensionalized as  $T/T_\infty$ . 25 levels from 0.9 to 2.8.

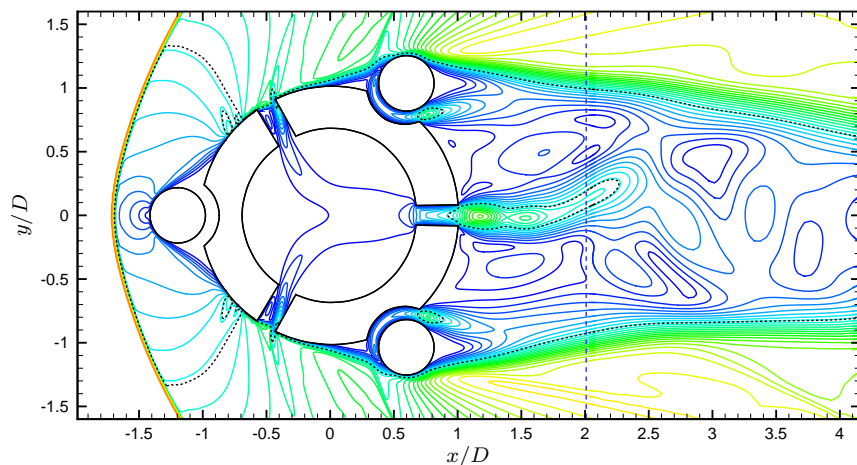


(b) Mach number contour. 30 levels from 0.1 to 3.3. Sonic contour shown as - - -.

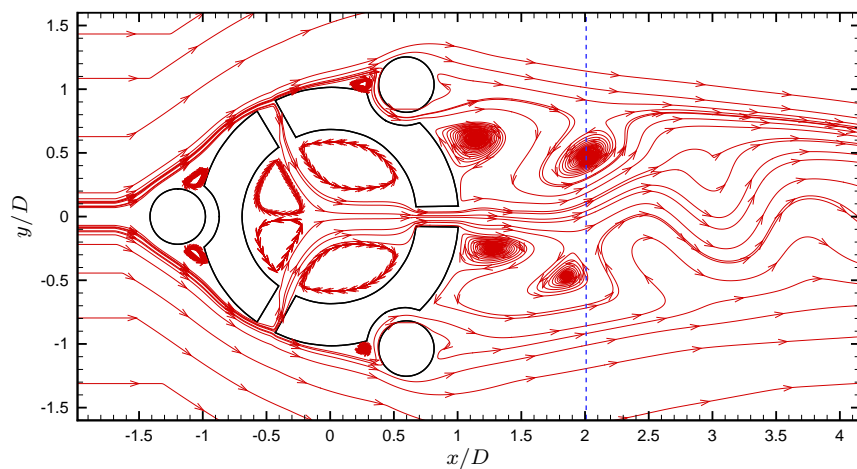
Figure 15. Temperature and Mach number contours for flow over the Ubuntu logo. First refinement zone edge - - -. Second refinement zone edge - - -.



(a) Temperature contour. Non-dimensionalized as  $T/T_\infty$ . 25 levels from 0.9 to 2.8.

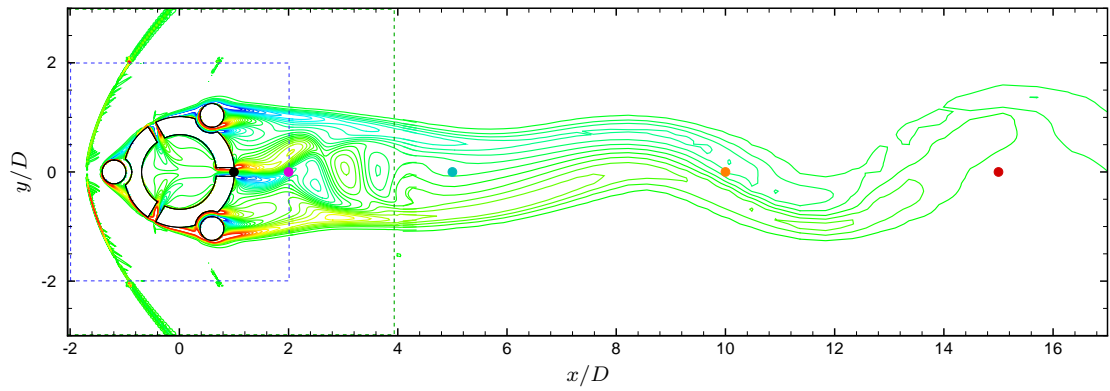


(b) Mach number contour. 30 levels from 0.1 to 3.3. Sonic contour shown as - - -.

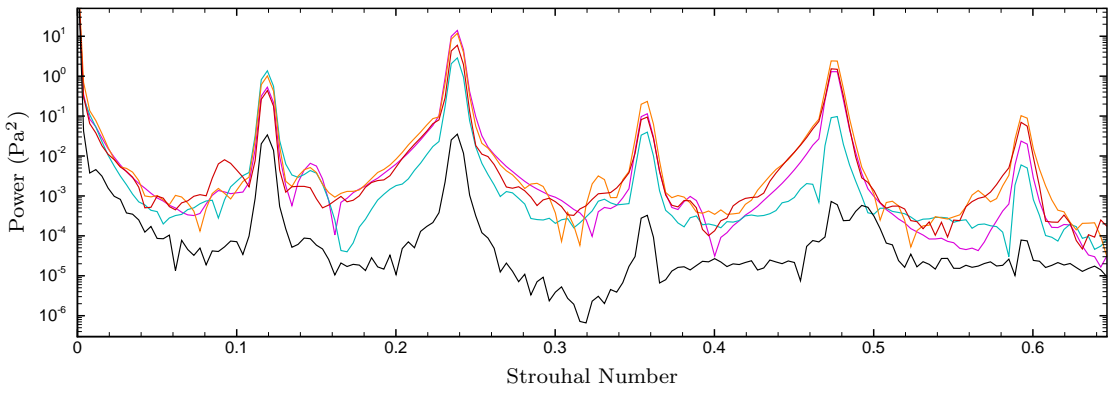


(c) Streamlines.

Figure 16. Flow variable contours and streamlines near the Ubuntu logo. Second refinement zone edge - - -.



(a) Vorticity contour. Colored dots denote the location of pressure probes. First refinement zone edge - - -. Second refinement zone edge - - -.



(b) FFT of the pressure history record at each probe. The line color corresponds to the probe color in Figure (a).

**Figure 17. Frequency analysis results for flow over the Ubuntu logo.**

Freestream Mach number	$M_\infty$	5.93
Freestream velocity	$u_\infty$	873 m/s
Freestream pressure	$p_\infty$	0.37 kPa
Freestream temperature	$T_\infty$	53.9 K
Stagnation pressure	$p_0$	551.58 kPa
Stagnation temperature	$T_0$	433 K
Wall temperature	$T_{wall}$	298.2 K
Freestream unit Reynolds number	$Re_\infty$	$5.94 \times 10^6 \text{ m}^{-1}$
Undisturbed boundary-layer thickness	$\delta$	9.23 mm
Ratio of roughness height to boundary-layer thickness	$k/\delta$	1.10
Ratio of roughness diameter to boundary-layer thickness	$D/\delta$	0.647

Table 2. Flow conditions for cylindrical roughness simulation.

peaks are harmonics of the first.

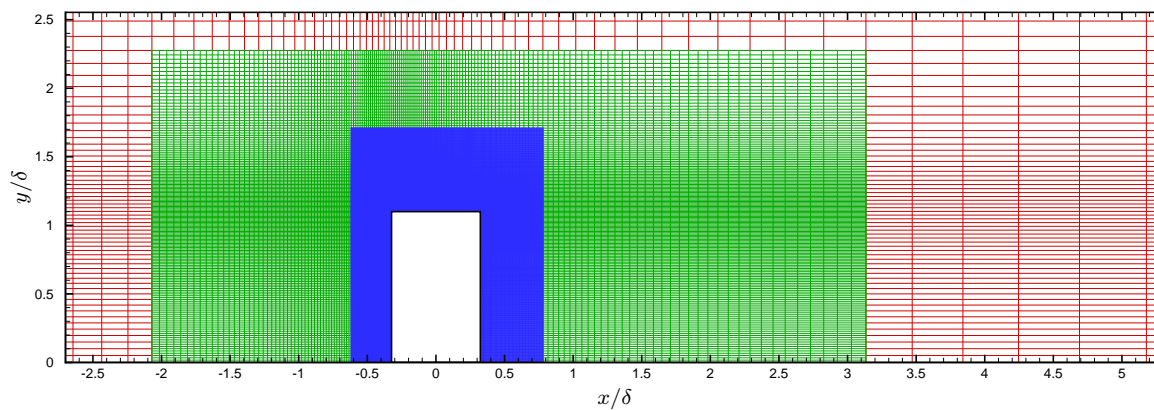
#### IV.D. Cylindrical Roughness

With the combined multi-zone and cut-cell code tested, work has begun on reproducing the results from the Boeing/AFOSR Mach 6 quiet wind tunnel at Purdue University. The wind tunnel is a Ludwig tube capable of generating quiet Mach 6 flow and is maintained by Professor Steven Schneider.<sup>34</sup> Wheaton and Schneider<sup>19</sup> have recently measured a 21 kHz instability in Pitot probe and hot-wire measurements for Mach 6 flow over a cylindrical roughness element with a height of 10.2 mm and a diameter of 5.97 mm. The undisturbed boundary layer had a thickness of approximately 9.23 mm. Ward et al.<sup>35</sup> measured the same instability with flush-mounted pressure transducers on the nozzle wall. The goal of the current simulation is to reproduce these results and to investigate the source of the instability. Due to difficulties in simulating the entire wind tunnel, the tunnel geometry was modeled as a flat plate. Although the geometry has changed, the same flow conditions as the Purdue wind tunnel have been used. The flow conditions used in the simulation come from Wheaton and Schneider and are given in Table 2.

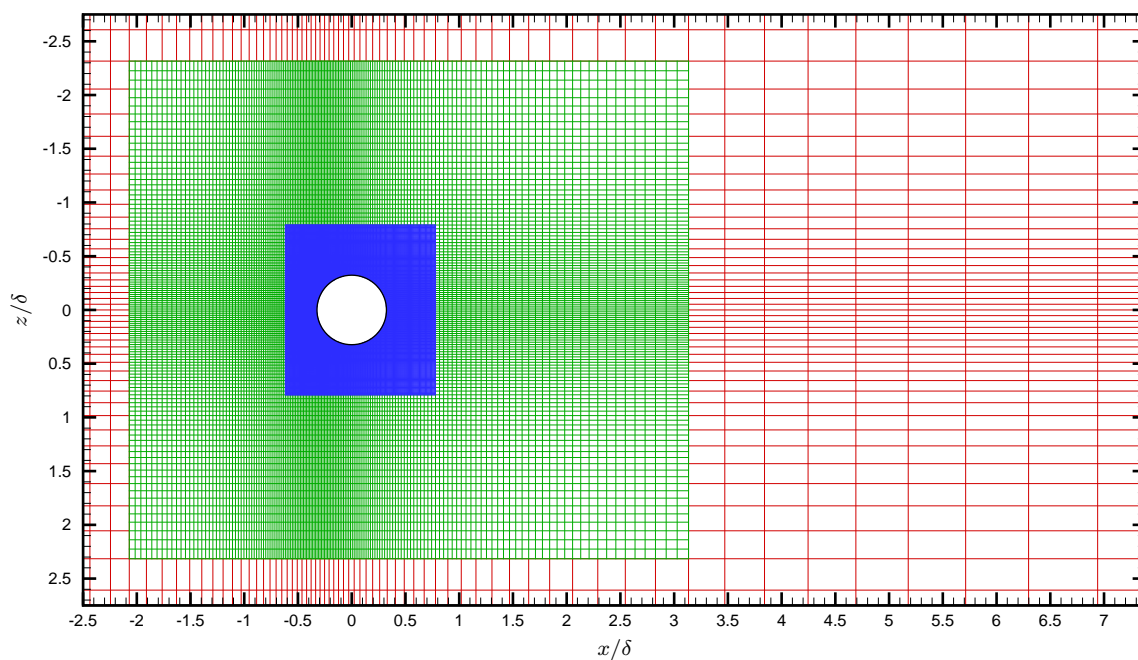
A coarse grid and two refinement grids were used for this simulation. The grids in the vicinity of the roughness are shown in Figure 18. Only a portion of the grid is shown in the figure. The full domain starts at  $x/\delta = -20$  and ends at  $x/\delta = 25$ . The top of the domain is located at  $y/\delta = 5$  and the domain half width is  $W/\delta = 7.5$ . The coarse grid has 200 points in the  $x$  direction, 140 points in the  $y$  direction, and 121 points in the  $z$  direction. The grids are clustered near the front of the roughness in the  $x$  direction, near the top of the roughness in the  $y$  direction, and near the center of the roughness in the  $z$  direction. The same boundary conditions as the hyperbolic roughness are used here except the wall is now isothermal instead of adiabatic.

Figure 19 shows the temperature contours at the  $z/\delta = 0$  plane. The flow has become unsteady but the flow field has not reached a statistically stationary state. The flow downstream of the roughness element is still changing significantly with time. Since the entire flow field has not reached a statistically stationary state, a frequency analysis of the instability has not been performed yet. However, the flow near the roughness element is no longer undergoing large scale changes. This allows preliminary results to be compared with previously published work from other researchers.

Figure 20 shows a comparison of the streamlines in front of the roughness element for the current simulation and a simulation performed at similar condition from Wheaton et al.<sup>36</sup> The vortical structures from the two simulations seem to match very well. Figure 21 shows the surface streamlines and wall pressure for the current simulation and a simulation performed by Bartkowicz et al.<sup>18</sup> The streamlines show the separation and re-attachment lines created by the vortices shown in Figure 20. Upstream of the roughness, the results in Figure 21 appear very similar. To the sides and downstream of the roughness, the streamlines begin to show differences. This may be due to transient effects from the initial condition for the current simulation. Since the simulation has not reached a statistically stationary state, the initial transients are still present. The simulation is still underway and more results will be presented at a future time.



(a)  $x - y$  plane at  $z/\delta = 0$



(b)  $x - z$  plane at  $y/\delta = 0$

Figure 18. Grid in the vicinity of the three-dimensional cylindrical roughness element. Points inside the roughness element are not shown. Coarse grid shown in red. First refinement grid with three times the resolution shown in green. Second refinement grid with an additional three times increase in resolution shown in blue. Only every second point shown in all directions.

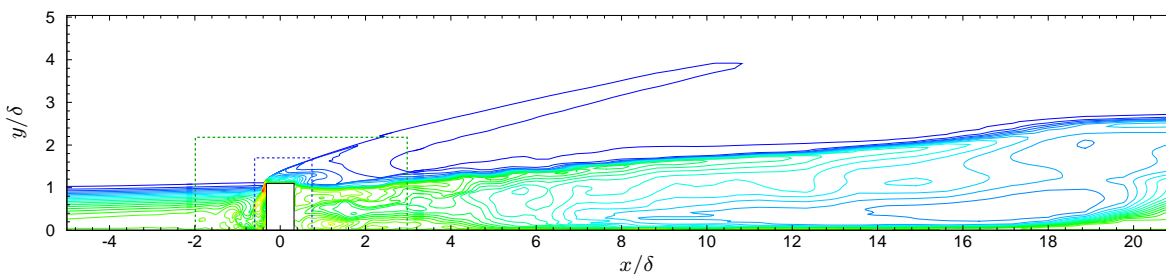
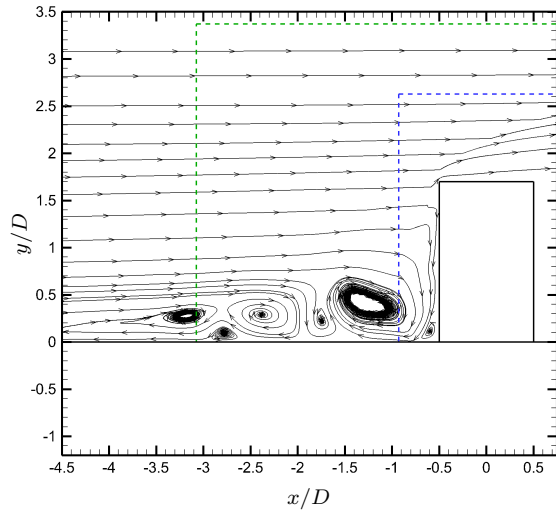
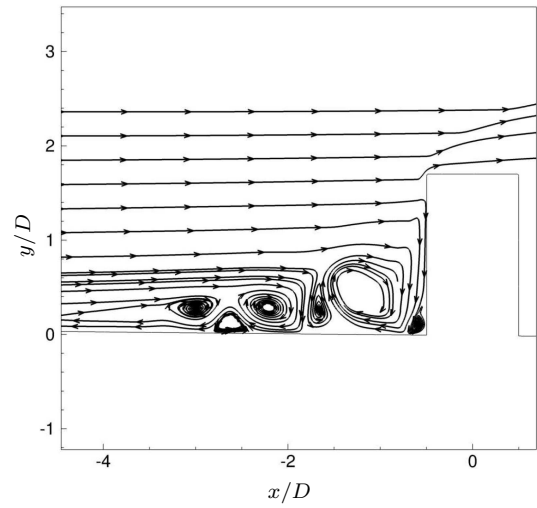


Figure 19. Temperature contours near cylindrical roughness at  $z/\delta = 0$  plane. Non-dimensionalized as  $T/T_\infty$  with 30 levels from 1.1 to 8.8. First refinement zone edge - - -; Second refinement zone edge - - -.

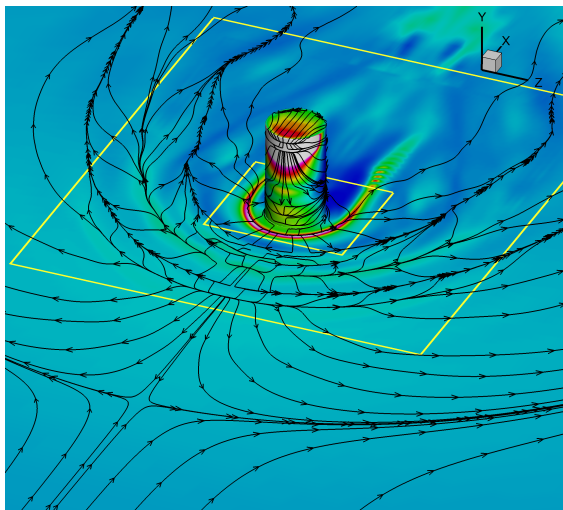


(a) Current simulation. First refinement zone edge - - -; Second refinement zone edge - - -.

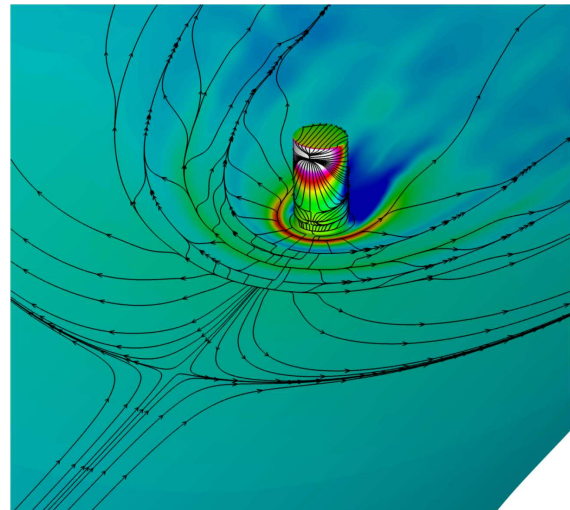


(b) Results from Wheaton et al.<sup>36</sup>

**Figure 20. Comparison of streamlines in  $z/\delta = 0$  plane for flow over cylindrical roughness.**



(a) Current simulation. Pressure plotted as  $p/p_\infty$  with contour levels varying from 0.4 to 5.0. Refinement grid edges shown as yellow rectangles.



(b) Results from Bartkovicz et al.<sup>18</sup>

**Figure 21. Comparison of surface streamlines and pressure contours for flow over cylindrical roughness.**

## V. Conclusion

Results were presented for a new code designed to perform high-order simulations of high-speed flows over arbitrary geometries. The code utilizes a cut-cell method to model complex geometries on a simple Cartesian grid. The code also uses a multi-zone refinement method to provide extra control over the placement of grid points. The cut-cell method was confirmed to provide globally fourth-order convergence when combined with the codes fifth-order interior scheme. It was also shown that the multi-zone method does not reduce the order of the interior scheme. The combination of the cut-cell and multi-zone refinement methods should result in a globally fourth-order scheme.

The code was validated by simulating subsonic flow over a cylinder and supersonic flow over an isolated roughness element constructed from hyperbolic tangents. Results from both simulations compare well with previously published results. To further test the capabilities of the code for flows involving complex geometries, supersonic flow over the Ubuntu logo was simulated. There are no results to compare with, but the results do not appear to have any obvious errors.

Based on these results, simulations for the problem of interest have begun. Mach 6 flow over an isolated cylindrical roughness element located on a flat plate are currently underway. Preliminary results were presented and found to match well with results from other researchers. Once the simulation reaches a statistically stationary state, further analysis of the flow will be performed and presented at a future date.

## Acknowledgments

The authors gratefully acknowledge support by the NASA Fundamental Aeronautics Program, under cooperative agreement NNX07AC39A, monitored by Dr. Meelan Choudhari and the partial support of the AFOSR/NASA National Center for Hypersonic Research in Laminar-Turbulent Transition headed by Professor W. Saric at Texas A&M University. The computer time for this work was provided by the NASA Ames Research Center Advanced Supercomputing Division, and the Extreme Science and Engineering Discovery Environment (XSEDE) supported by National Science Foundation.

## References

- <sup>1</sup>Berry, S. and Horvath, T., "Discrete Roughness Transition for Hypersonic Flight Vehicles," *45th AIAA Aerospace Sciences Meeting and Exhibit*, AIAA Paper 2007-307, Jan 2007.
- <sup>2</sup>Schneider, S. P., "Effects of Roughness on Hypersonic Boundary-Layer Transition," *Journal of Spacecraft and Rockets*, Vol. 45, No. 2, Mar-Apr 2008, pp. 193-209.
- <sup>3</sup>Tumin, A. and Reshotko, E., "Spatial theory of optimal disturbances in boundary layers," *Physics of Fluids*, Vol. 13, No. 7, July 2001, pp. 2097-2104.
- <sup>4</sup>White, E. and Reshotko, E., "Roughness-Induced Transient Growth in a Flat-Plate Boundary Layer," *40th AIAA Aerospace Sciences Meeting & Exhibit*, AIAA Paper 2002-0138, Jan 2002.
- <sup>5</sup>White, E. and Ergin, F., "Receptivity and Transient Growth of Roughness-Induced Disturbances," *33rd AIAA Fluid Dynamics Conference and Exhibit*, AIAA Paper 2003-4243, June 2003.
- <sup>6</sup>White, E. B., Rice, J. M., and Gokhan Ergin, F., "Receptivity of stationary transient disturbances to surface roughness," *Physics of Fluids*, Vol. 17, No. 6, June 2005, pp. 064109.
- <sup>7</sup>Fischer, P. and Choudhari, M., "Numerical simulation of roughness-induced transient growth in a laminar boundary layer," *34th AIAA Fluid Dynamics Conference and Exhibit*, AIAA Paper 2004-2539, June 2004.
- <sup>8</sup>Choudhari, M. and Fischer, P., "Roughness-Induced Transient Growth," *35th AIAA Fluid Dynamics Conference and Exhibit*, AIAA Paper 2005-4765, June 2005.
- <sup>9</sup>Reshotko, E. and Tumin, A., "Role of transient growth in roughness-induced transition," *AIAA Journal*, Vol. 42, No. 4, Apr 2004, pp. 766-770.
- <sup>10</sup>Reda, D. C., "Correlation of Noretip Boundary-Layer-Transition Data Measured In Ballistics-Range Experiments," *AIAA Journal*, Vol. 19, No. 3, 1981, pp. 329-339.
- <sup>11</sup>Reda, D. C., "Review and Synthesis of Roughness-Dominated Transition Correlations For Reentry Applications," *Journal of Spacecraft And Rockets*, Vol. 39, No. 2, Mar 2002, pp. 161-167.
- <sup>12</sup>Acarlar, M. and Smith, C., "A Study of Hairpin Vortices in a Laminar Boundary Layer . Part 1. Hairpin Vortices Generated by a Hemisphere Protuberance," *Journal of Fluid Mechanics*, Vol. 175, Feb 1987, pp. 1-41.
- <sup>13</sup>Ergin, F. G. and White, E. B., "Unsteady and Transitional Flows Behind Roughness Elements," *AIAA Journal*, Vol. 44, No. 11, Nov 2006, pp. 2504-2514.
- <sup>14</sup>Chang, C.-L. and Choudhari, M., "Hypersonic Viscous Flow over Large Roughness Elements," *47th AIAA Aerospace Sciences Meeting and Exhibit*, AIAA Paper 2009-0173, 2009.
- <sup>15</sup>Papamoschou, D. and Roshko, A., "The Compressible Turbulent Shear-Layer: An Experimental Study," *Journal of Fluid Mechanics*, Vol. 197, Dec 1988, pp. 453-477.

<sup>16</sup>Danehy, P., Bathel, B., Ivey, C., Inman, J., and Jones, S., "NO PLIF Study of Hypersonic Transition Over a Discrete Hemispherical Roughness Element," *47th AIAA Aerospace Sciences Meeting including The New Horizons Forum and Aerospace Exposition*, AIAA Paper 2009-394, Jan 2009.

<sup>17</sup>Chang, C.-L., Choudhari, M., and Li, F., "Numerical Computations of Hypersonic Boundary-Layer over Surface Irregularities," *48th AIAA Aerospace Sciences Meeting Including the New Horizons Forum and Aerospace Exposition*, AIAA Paper 2010-1572, Jan 2010.

<sup>18</sup>Bartkowicz, M. D., Subbareddy, P., and Candler, G., "Numerical Simulations of Roughness Induced Instability in the Purdue Mach 6 Wind Tunnel," *40th Fluid Dynamics Conference and Exhibit*, AIAA Paper 2010-4723, 2010.

<sup>19</sup>Wheaton, B. M. and Schneider, S. P., "Roughness-Induced Instability in a Laminar Boundary Layer at Mach 6," *48th AIAA Aerospace Sciences Meeting*, AIAA Paper 2010-1574, 2010.

<sup>20</sup>Wheaton, B. and Schneider, S., "Roughness-Induced Instability in a Hypersonic Laminar Boundary Layer," *AIAA Journal*, Vol. 50, No. 6, 2012, pp. 1245–1256.

<sup>21</sup>Duan, Z., Xiao, Z., and Fu, S., "Direct Numerical Simulation of Hypersonic Transition Induced by a Cylindrical Roughness Element," *43rd Fluid Dynamics Conference*, AIAA Paper 2013-3112, 2013.

<sup>22</sup>Duan, L., Wang, X., and Zhong, X., "A high-order cut-cell method for numerical simulation of hypersonic boundary-layer instability with surface roughness," *J. Comput. Phys.*, Vol. 229, No. 19, 2010, pp. 7207 – 7237.

<sup>23</sup>Greene, P., Eldredge, J., Zhong, X., and Kim, J., "Numerical Study of Hypersonic Flow Over an Isolated Roughness with a High-Order Cut-Cell Method," *41st AIAA Fluid Dynamics Conference and Exhibit*, AIAA Paper 2011-3249, 2011.

<sup>24</sup>Ren, Y.-X., Liu, M., and Zhang, H., "A characteristic-wise hybrid compact-WENO scheme for solving hyperbolic conservation laws," *Journal of Computational Physics*, Vol. 192, No. 2, 2003, pp. 365 – 386.

<sup>25</sup>Henrick, A. K., Aslam, T. D., and Powers, J. M., "Mapped weighted essentially non-oscillatory schemes: Achieving optimal order near critical points," *Journal of Computational Physics*, Vol. 207, No. 2, 2005, pp. 542 – 567.

<sup>26</sup>Zhong, X. L., "High-order finite-difference schemes for numerical simulation of hypersonic boundary-layer transition," *Journal of Computational Physics*, Vol. 144, No. 2, Aug 1998, pp. 662–709.

<sup>27</sup>Jiang, G. and Shu, C., "Efficient Implementation of Weighted ENO Schemes," *J. Comput. Phys.*, Vol. 126, No. 1, 1996, pp. 202–228.

<sup>28</sup>Shen, C., Qiu, J.-M., and Christlieb, A., "Adaptive mesh refinement based on high order finite difference WENO scheme for multi-scale simulations," *J. Comput. Phys.*, Vol. 230, No. 10, 2011, pp. 3780–3802.

<sup>29</sup>Thompson, K. W., "Time-Dependent Boundary-Conditions For Hyperbolic Systems," *Journal of Computational Physics*, Vol. 68, No. 1, Jan 1987, pp. 1–24.

<sup>30</sup>Williamson, C., "Vortex dynamics in the cylinder wake," *Annual Review Of Fluid Mechanics*, Vol. 28, 1996, pp. 477–539.

<sup>31</sup>Marxen, O. and Iaccarino, G., "Numerical Simulation of the Effect of a Roughness Element on High-Speed Boundary-Layer Instability," *38th Fluid Dynamics Conference and Exhibit*, AIAA Paper 2008-4400, June 2008.

<sup>32</sup>Xu, S. and Martin, M., "Assessment of inflow boundary conditions for compressible turbulent boundary layers," *Physics of Fluids*, Vol. 16, No. 7, July 2004, pp. 2623–2639.

<sup>33</sup>Canonical Ltd, "Ubuntu," <http://www.ubuntu.com/>.

<sup>34</sup>Schneider, S. P., "Fabrication and testing of the Purdue Mach-6 quiet-flow Ludwig tube," *38th Aerospace Sciences Meeting & Exhibit*, AIAA Paper 2000-0295, Jan 2000.

<sup>35</sup>Ward, C., Wheaton, B., Chou, A., Gilbert, P., Steen, L., and Schneider, S., "Boundary-Layer Transition Measurements in a Mach-6 Quiet Tunnel," *40th Fluid Dynamics Conference and Exhibit*, AIAA Paper 2010-4721, 2010.

<sup>36</sup>Wheaton, B. M., Bartkowicz, M. D., Subbareddy, P., Schneider, S., and Candler, G., "Roughness-Induced Instabilities at Mach 6: A Combined Numerical and Experimental Study," *41st AIAA Fluid Dynamics Conference and Exhibit*, AIAA Paper 2011-3248, June 2011.